THE ASTROPHYSICAL JOURNAL, 555:572–584, 2001 July 10

GALAXY HALO MASSES FROM GALAXY-GALAXY LENSING[1]

GILLIAN WILSON,[2,3] NICK KAISER,[2] GERARD A. LUPPINO,[2] AND LENNOX L. COWIE[2]

Received 2000 July 12; accepted 2001 March 2

ABSTRACT

We present measurements of the extended dark halo profiles of bright early-type galaxies at redshifts $0.1 < z < 0.9$ obtained via galaxy-galaxy lensing analysis of images taken at the Canada-France-Hawaii Telescope using the UH8K CCD mosaic camera. Six $0.^{\circ}5 \times 0.^{\circ}5$ fields were observed for a total of 2 hr each in I and V, resulting in catalogs containing $\sim$20,000 galaxies per field. We used $V-I$ color and I magnitude to select bright early-type galaxies as the lens galaxies, yielding a sample of massive lenses with fairly well-determined redshifts and absolute magnitudes $M \sim M_* \pm 1$. We paired these with faint galaxies lying at angular distances $20'' < \theta < 60''$, corresponding to physical radii of $26 < r < 77\ h^{-1}$ kpc ($z = 0.1$) and $105 < r < 315\ h^{-1}$ kpc ($z = 0.9$), and computed the mean tangential shear $\gamma_T(\theta)$ of the faint galaxies. The shear falls off with radius roughly as $\gamma_T \propto 1/\theta$ as expected for flat rotation curve halos. The shear values were weighted in proportion to the square root of the luminosity of the lens galaxy. This is optimal if the halo mass at a given radius varies as $M \propto \sqrt{L}$, as is the case at smaller radii, and in this context our results give a value for the average mean rotation velocity of an L_* galaxy halo at $r \sim 50$–$200\ h^{-1}$ kpc of $v_* = 238^{+27}_{-30}$ km s^{-1} for a flat lambda ($\Omega_{m0} = 0.3$, $\Omega_{\lambda 0} = 0.7$) cosmology ($v_* = 269^{+34}_{-39}$ km s^{-1} for Einstein–de Sitter) and with little evidence for evolution with redshift. These halo masses are somewhat (2–3 times) lower than a simple perfectly flat rotation curve extrapolation from smaller scale dynamical measurements. They are also considerably lower than the masses of halos found from the best-studied X-ray halos. They do, however, agree extremely well with the masses of halos of the same abundance in lambda-CDM simulations. We find a mass-to-light ratio of $M/L_B \simeq 121 \pm 28h(r/100\ h^{-1}$ kpc) (for L_* galaxies) and these halos constitute $\Omega \simeq 0.04 \pm 0.01(r/100\ h^{-1}$ kpc) of closure density.

Subject headings: cosmology: observations — dark matter — galaxies: evolution — galaxies: halos — galaxies: luminosity function, mass function — gravitational lensing

1. INTRODUCTION

The existence of extended dark matter halos with approximately flat rotation curves around galaxies is now well established. At small scales, the halo mass can be measured from stellar velocity dispersions and rotation curves and globular cluster kinematics (e.g., reviews by Faber & Gallagher 1979; Trimble 1987). Spiral galaxy H I rotation curves (Bosma 1981) extend this and indicate $M \propto r$ out to tens of kiloparsecs. Relative motions of faint satellites (Bahcall & Tremaine 1981; Zaritsky et al. 1997) or pairs of galaxies (Turner 1976; Jing, Mo, & Boerner 1998) analyzed statistically extend this to larger scales, and at still larger scales the cosmic virial theorem analysis (Davis & Peebles 1983) shows that relative motions remain flat or slowly rising to scales of a few Mpc, suggesting that the average mass around a galaxy continues to rise roughly in proportion to radius. Galaxy clustering measurements show that the excess *light* around a galaxy is $L_{\rm excess}(<r) \simeq 4\pi\xi(r)\mathscr{L}r^3$ where $\mathscr{L}$ is the mean luminosity density. This also grows roughly in proportion to radius. The excess light is equal to L_* at a radius of $r \sim 400\ h^{-1}$ kpc. On scales larger than this, one is dealing not with individual halos but with the collective mass of collections of neighboring galaxies. Here we shall restrict attention to smaller scales where it is reasonable to interpret the results as probing relatively stable and virialized halos of individual galaxies.

The halos of early-type galaxies can also be probed via X-ray–emitting hot gas. This is valuable as it removes some of the uncertainty regarding orbital anisotropy in the above analyses. Unfortunately, the halos are very faint, and only a handful of galaxies have the resolved flux and temperature data required (Kim & Fabbiano 1995; Trinchieri, Fabbiano, & Kim 1997). In the best-studied case (NGC 4636) (Mushotzky et al. 1994; Trinchieri et al. 1994), the halo is very massive indeed $M(<100$ kpc$) \simeq 5.1 \times 10^{12}\ M_\odot$. The line-of-sight stellar velocity dispersion for this galaxy is $\sigma \simeq 191$ km s^{-1}—comparable to the mean value $\sim$210 km s^{-1} for L_* galaxies (Fukugita & Turner 1991)—corresponding to a rotation velocity $\sim$330 km s^{-1} for the luminous region, whereas the X-ray mass at 100 kpc gives a rotation velocity of 470 km s^{-1}.

The mass of galaxy halos at radii $\sim$100–300 kpc is of considerable importance both in the accounting of the matter content of the universe and in testing cosmological theories (which are typically finely tuned to match the properties of massive galaxy clusters). However, the dynamical measurements suffer from systematic modeling uncertainties, and it is difficult to know whether halos like that of NGC 4636 are typical of ordinary bright ellipticals.

Gravitational lensing offers an alternative probe of the dark matter around galaxies. The manifestation of lensing we shall exploit here is the weak "galaxy-galaxy lensing" effect; the distortion of shapes of (typically faint) background galaxies seen near (typically brighter) foreground galaxies. Clusters of galaxies have traditionally been the

[1] Based on observations with the Canada-France-Hawaii Telescope, which is operated by the National Research Council of Canada, le Centre National de la Recherche Scientifique de France, and the University of Hawaii.

[2] Institute for Astronomy, University of Hawaii, 2680 Woodlawn Drive, Honolulu, HI 96822.

[3] Physics Department, Brown University, 182 Hope Street, Providence, RI 02912; gillian@het.brown.edu.

primary target of weak lensing studies (see Mellier 1999 for a review). Individual galaxy masses are far more difficult to measure because of their being less massive and, hence, yielding a smaller lensing signal relative to the noise. However, by stacking pairs of galaxies it is possible to beat down the noise and measure the total average halo profile.

In galaxy-galaxy lensing one measures the mean tangential shear of faint "source" galaxies averaged over source-lens pairs binned by angular separation:

$$\gamma_T(\theta) = -\frac{\sum_{\rm pairs} W_l W_s M_{\alpha ij}\theta_i\theta_j\hat{\gamma}_\alpha/\theta^2}{\sum_{\rm pairs} W_l W_s}\,, \tag{1}$$

where $\hat{\gamma}_\alpha$, for $\alpha = 1, 2$, is the shear estimate for the source galaxy, θ is the projected angular separation of the lens and source, W_l, W_s are weights for the lens and source, and the two constant matrices M_1, M_2 are

$$M_{1lm} \equiv \begin{bmatrix} 1 & 0 \\ 0 & -1 \end{bmatrix}, \quad M_{2lm} \equiv \begin{bmatrix} 0 & 1 \\ 1 & 0 \end{bmatrix}. \tag{2}$$

The expectation value of the mean tangential shear is related to the mean excess dimensionless mass surface density $\kappa(\theta)$ by

$$\langle\gamma_T(\theta)\rangle = -\frac{\partial\overline{\kappa}}{\partial\ln\theta^2}\,, \tag{3}$$

with

$$\overline{\kappa}(\theta) \equiv \frac{1}{\pi\theta^2}\int_{|\theta'|<\theta} d^2\theta'\kappa(\theta') \tag{4}$$

(Kaiser et al. 1994). The dimensionless excess surface density is, in turn, related to the galaxy-mass cross-correlation function $\xi_{g\rho}$ by

$$\begin{aligned}\kappa(\theta) = \frac{4\pi G}{c^2}&\int dz_l\, n_l(z_l) D_l\langle\beta(z_l)\rangle \\ &\times\int dM_L\,\Phi(M_l;\, z_l)\langle W_l(M_l,\, z_l)\rangle \\ &\times\int dy\,\xi_{g\rho}(\sqrt{y^2 + D_l^2\,\theta^2};\, M_l,\, z_l) \\ &\times\left[\int dz_l\, n_l(z_l)\int dM_l\,\Phi(M_l;\, z_l)\langle W_l(M_l,\, z_l)\rangle\right]^{-1},\end{aligned} \tag{5}$$

where $n_l(z)$ is the redshift distribution for the lens galaxies; $\Phi(M;\, z)$ is the absolute magnitude distribution at redshift z; $\xi_{g\rho}(r;\, M,\, z)$ is the galaxy-mass cross-correlation, defined as the mean physical density at a physical distance r from a lens galaxy, parameterized by the absolute magnitude and redshift. The quantity $\langle W_l(M,\, z)\rangle$ is the mean weight for galaxies of a given absolute magnitude and redshift. The angular diameter distance is $D_l \equiv a_0\,\omega_l/(1 + z_l)$, where ω is comoving distance measured in units of the current curvature scale $a_0 = c/[H_0(1 - \Omega_{m0} - \Omega_{\lambda 0})^{1/2}]$. The dimensionless quantity $\langle\beta(z_l)\rangle$ is defined as

$$\langle\beta(z_l)\rangle \equiv \frac{\int_0^\infty dz_s\, n_s(z_s)\langle W_s(z_s)\rangle\beta(z_l,\, z_s)}{\int_0^\infty dz_s\, n_s(z_s)\langle W_s(z_s)\rangle}\,, \tag{6}$$

where $n_s(z)$ is the redshift distribution of the source galaxies, $\langle W_s(z_s)\rangle$ is the mean weight for source galaxies at redshift z_s, and where, finally,

$$\beta(z_l,\, z_s) \equiv \max\,[0,\, \sinh\,(\omega_s - \omega_l)/\sinh\,(\omega_s)]\,. \tag{7}$$

Physically, $\beta(z_l,\, z_s)$ is the ratio of the distortion induced by a lens at redshift z_l in an object at finite distance $\omega(z_s)$ relative to that for a fictitious source at infinite distance.

For the special case of a spatially flat cosmology, $\omega \to 0$ and $a_0 \to \infty$, but such that their product remains finite. In that case $\sinh\,\omega \to \omega$, and $\langle\beta\rangle \equiv \langle\max\,(0,\, 1 - \omega_l/\omega_s)\rangle$. For the limiting case of $\Omega_m = 1$, $\Omega_\lambda = 0$, $\omega(z) = 2[1 - 1/(1 + z)^{1/2}]$ and, in the other extreme, for $\Omega_m \to 0$, $\Omega_\lambda \to 1$, $\omega(z) = z$.

Equations (7), (5), (4), and (3) provide a direct relationship between observable $\langle\gamma_T\rangle$ and the cosmologically interesting quantity $\xi_{g\rho}$. They allow one to compute the expected tangential shear given a cosmological model, a theoretical $\xi_{g\rho}$, measured redshift distributions $n_s(z)$, $n_l(z)$ for source and lens galaxies, and user-supplied weights. The latter ideally should be determined from the image quality for the sources and from the brightness of the lens galaxies in such a way as to maximize the signal-to-noise ratio (S/N), but the results above are valid for arbitrary weights.

One can also calculate the variance in the mean tangential shear, and combining this with the formalism above yields the expected S/N. This exercise shows that the S/N is rather poor if galaxies are divided into lens and source samples solely on magnitude. This is because the range of redshift at a given apparent magnitude is large, so there is a large variation in bright galaxy absolute luminosity and therefore in the mass. There is also a large range in β values. Photometric redshifts are useful in this regard to tighten up the distribution of foreground lenses and allow one to boost the S/N by giving weight preferentially to the more massive galaxies.

The above equations are quite general. For the special case of a power-law galaxy-mass correlation function $\xi_{g\rho}(r) \propto r^{-\gamma}$, then $\langle\gamma_T(\theta)\rangle \propto \theta^{1-\gamma}$ with a constant of proportionality that is computable from the lens, source redshift distributions, etc. Specializing further, for a flat rotation curve object, the shear is given by

$$\begin{aligned}\gamma_T(\theta) &= \pi(v/c)^2\langle\beta(z_l)\rangle/\theta \\ &= 0.93(v/360\ \text{km s}^{-1})^2(1''/\theta)\langle\beta(z_l)\rangle\,.\end{aligned} \tag{8}$$

This equation provides a convenient rule of thumb to convert between measured shear values and an equivalent rotation velocity. Similarly, if $\xi_{g\rho} \propto r^{-2}$, we can characterize the mean halo profile in terms of an equivalent mean rotation velocity, which is convenient when one comes to compare with dynamical measurements on smaller scales. (The fiducial rotation velocity of 360 km s^{-1} is that obtained for an L_* early-type galaxy from Faber-Jackson measurements [Fukugita & Turner 1991].) We return to discuss the value of rotation velocity as measured by a variety of techniques in § 4.

Early photographic measurements (Tyson et al. 1984) gave an essentially null detection of tangential shear that seemed to rule out extended massive halos, though the upper limit was subsequently revised upward (Kovner & Milgrom 1987; Kaiser 1991). The first detection of galaxy-galaxy lensing was by Brainerd, Blandford, & Smail (1996). Since then, a number of groups have presented estimates of galaxy-galaxy lensing, either from Hubble Deep Field observations (Dell'Antonio & Tyson 1996; Griffiths et al.

1996; Hudson et al. 1998), from observations of the rich cluster AC 114 (Natarajan et al. 1998), or from the Sloan Digital Sky Survey (Fischer et al. 2000). These results demonstrate the practicality of the approach, but there are some uncertainties concerning their calibration.

In this paper, we investigate galaxy-galaxy lensing using data collected at the Canada-France-Hawaii Telescope (CFHT) with the UH8K camera. Our analysis differs somewhat from other works in that we focus on bright early-type galaxy halos, as these are the only class of objects with redshifts that can be reliably determined from two-passband photometry. However, while early-type galaxies contribute only 30%–50% to the total luminosity density, dynamical studies of the local universe show that an L_{*B} elliptical has about four times the mass (at a given radius) as an L_{*B} spiral (Fukugita & Turner 1991), and these objects are expected to dominate the lensing signal at all redshifts.

The outline of the paper is as follows. In § 2 we describe the data and the selection of lens and background galaxies. In § 3, we present tangential shear measurements for lens galaxies over a wide range of redshifts. To facilitate the comparison with other studies and with predictions from simulations, we characterize the halo profiles in terms of the equivalent rotation velocity for an L_* galaxy. In § 4 we discuss our results. We calculate the mass-to-light ratio of an L_* early-type galaxy and the contribution of early types to the closure density. We also compare our values to other lensing studies, X-ray measurements, and to the masses of simulated halos of the same abundance. In § 5 we briefly summarize our conclusions. We assume a flat lambda ($\Omega_{m0} = 0.3$, $\Omega_{\lambda 0} = 0.7$) cosmology with $H_0 = 100\ h$ km s^{-1} Mpc^{-1} throughout unless explicitly stated otherwise.

2. THE DATA AND GALAXY SAMPLES

2.1. *Data Acquisition and Reduction*

The data were taken at the 3.6 m CFHT telescope using the 8192 × 8192 pixel UH8K camera at prime focus. The field of view of this camera is ∼30′ with pixel size 0.″207. The data (six pointings) used in the analysis were acquired as part of an ongoing project, the principle aim of which is to investigate the cosmic shear pattern caused by gravitational lensing from the large-scale structure of the universe. Table 1 gives an overview of the data, describing the field name, center, and seeing for each pointing. This is the second in a series of papers describing results from that project. Kaiser, Wilson, & Luppino (2001a, hereafter Paper I) presented estimates of cosmic shear variance on 2′–30′ scales. Here we focus on properties of massive galaxy halos at radii of 50–200 h^{-1} kpc. Forthcoming papers will address galaxy clustering and correlations between mass and light on cluster and group scales (Wilson, Kaiser, & Luppino 2001, Paper III in series). A full description of our catalogs will be presented in a later paper (G. Wilson & N. Kaiser 2001, in preparation). Further details of the data reduction pipeline may be found in Kaiser et al. (2001b) and an application to the MS0302 supercluster in Kaiser et al. (2001c). In brief, the data was dark-subtracted, flat-fielded, registered, and median-averaged. Weighted second-moment shapes and magnitudes of objects were measured using varying aperture photometry, and optimally weighted shear estimates for each galaxy, γ_α, were determined using the method described in Kaiser (2000).

2.2. *Lens Galaxy Sample*

Our analysis differs from other groups in that we use $V-I$ color to select a sample of bright early-type lens galaxies with reasonably well-determined redshifts. This allows us to focus on a single type of galaxy—though it obviously precludes drawing any useful conclusions about later type galaxies—and may allow useful constraints on the evolution of halos over time and on the profile.

To a first approximation, galaxies can be divided into spectral classes within which the galaxies have very similar, and largely luminosity independent, spectral energy distributions (SEDs). For each type, t, there is a color-redshift relation $c = c_t(z)$. With measurements of two colors (i.e., a minimum of three passbands), it should then generally be possible to determine both the spectral type and redshift. Here we have only fluxes in two passbands, but this is still sufficient to select a subset of galaxies—bright early types—and assign them approximate redshifts. This is because early-type galaxies are the reddest galaxies at a given redshift. Thus, if we select galaxies of some color c, we will see a superposition of early-type galaxies at redshift z_E such that $c = c_E(z_E)$ and later types at their appropriate, but considerably higher, redshift. An $L \sim L_*$ early-type galaxy will appear much brighter than an $L \sim L_*$ spiral galaxy, as we will see shortly, by about 3 mag, so with a judicious cut in red flux it should be possible to isolate a bright—and therefore presumably massive—early-type galaxy sample. To substantiate these comments, we first compute the expected contribution to the counts as a function of I magnitude for slices in color from galaxies of various types using the local 2dF luminosity function determination assuming no evolution. We compare these with our observed counts. We then test the technique with real high-redshift galaxies of Cowie (Cowie et al. 1994, 1996; Cowie, Songaila, & Barger 1999; G. Wilson, L. L. Cowie, A. J. Barger, & D. J. Burke 2001, in

TABLE 1

FIELD CENTERS AND SEEING

Field	Pointing	R.A. (J2000)	Decl. (J2000)	l	b	FWHM (I) (arcsec)	FWHM (V) (arcsec)
Lockman.....	1	10 52 43.0	57 28 48.0	149.28	53.15	0.83	0.85
	2	10 56 43.0	58 28 48.0	147.47	52.83	0.84	0.86
Groth	1	14 16 46.0	52 30 12.0	96.60	60.04	0.80	0.93
	3	14 09 00.0	51 30 00.0	97.19	61.57	0.70	0.85
1650	1	16 51 49.0	34 55 02.0	57.37	38.67	0.82	0.85
	3	16 56 00.0	35 45 00.0	58.58	37.95	0.85	0.72

NOTE.—Units of right ascension are hours, minutes, and seconds, and units of declination are degrees, arcminutes, and arcseconds.

preparation) and demonstrate the photometric redshift precision.

Given the SED f_ν for galaxies of type t, one can compute the color as a function of redshift $c_t(z)$. A narrow band of color of width dc around some color c then corresponds, for that type, to a range of redshift $dz = (dc_t/dz)^{-1}\,dc$ around $z = z_t(c)$, this being the inverse function defined such that $c_t[z_t(c)] = c$. If the color-redshift curve $c_t(z)$ is nonmonotonic, then the inverse function $z_t(c)$ will be multivalued. We define the type-specific luminosity function $\phi_t(L)$ such that the number of galaxies of type t in comoving volume d^3r and in an interval of width dL around L is

$$dn_t = \phi_t(L)dL\,d^3r\ . \tag{9}$$

Equivalently, the distribution over absolute magnitude, most often quoted in terms of B magnitudes, is

$$dn_t = \Phi_t(M_B)dM_B\,d^3r \tag{10}$$

with

$$\Phi_t(M_B) \equiv 0.4\ln(10)L\phi_t(L)\ . \tag{11}$$

The apparent magnitude in the I band is

$$m_I = M_B + 5\log\,[D_l(z)/10\mathrm{pc}] + K_{BIt}(z)\ , \tag{12}$$

where $D_l(z)$ is the luminosity distance and where $K_{BIt}(z) = K_{It}(z) - (M_B - M_I)_{t0}$ is the combination of the conventional K correction (for galaxy type t in the I band) and the rest-frame color for that type. At fixed color (and therefore fixed redshift) $dm_I = dM_B$, while the comoving volume element is

$$d^3r = D^2\,d\Omega\,dz\,\frac{dr}{dz}\ , \tag{13}$$

where $d\Omega$ is the solid angle, dr is a comoving radial distance element, and $D = D_l/(1+z)$ is the transverse comoving distance. The contribution to the counts from galaxies of type t and in an infinitesimal range of color dc is then, from equation (10),

$$\frac{dn_t}{d\Omega\,dm_I} = dcD^2\,\frac{dr}{dz}\left(\frac{dc_t}{dz}\right)^{-1} \times \Phi_t\left(m_I - 5\log\left\{\frac{D_l[z_t(c)]}{10\ \mathrm{pc}}\right\} - K_{BIt}[z_t(c)]\right). \tag{14}$$

In this model—a universal and nonevolving SED for each type—the counts at a given color are simply a superposition of scaled and shifted replicas of the various $\Phi_t(M_B)$. The counts for a finite range of color $c_1 < c < c_2$ are obtained by integrating (14) to give

$$\frac{dn_t}{d\Omega\,dm_I} = \int_{c_1<c_t(z)<c_2} dz\ D^2\left(\frac{dr}{dz}\right) \times \Phi_t\left\{m_I - 5\log\left[\frac{D_l(z)}{10\ \mathrm{pc}}\right] - K_{BIt}(z)\right\}, \tag{15}$$

which can readily be computed as a discrete sum given tabulated colors, K corrections as a function of redshift.

The counts for a set of narrow slices in color (chosen to correspond to a set of uniform width slices in redshift for early-type galaxies) are shown in Figure 1 (lower axis is apparent I magnitude and left axis is log counts—i.e., number of galaxies per square degree per magnitude). Also shown are predictions for the contribution to the counts according to equation (15) for various galaxy types according to the Schechter function model for local type-specific luminosity function

$$\phi_t(L)dL = \phi_{*t}\left(\frac{L}{L_{*t}}\right)^{\alpha_t} e^{-L/L_{*t}}\,\frac{dL}{L_{*t}}\ , \tag{16}$$

or, equivalently,

$$\Phi_t(M_B) \equiv 0.4\ln(10)\phi_{*t}\,10^{0.4(1+\alpha_t)(M_{B*t}-M_B)} \times \exp\,[-10^{0.4(M_{B*t}-M_B)}]\ , \tag{17}$$

with parameters ϕ_{*t}, α_t, and M_{B*t} (Table 2) determined from the 2dF redshift survey by Folkes et al. (1999) and with colors, K corrections, etc., computed using transmission functions for the UH8K system and SEDs from Coleman, Wu, & Weedman (1980) (2dF types Sab and types Sbc are combined into one group as K corrections for type Sab and are unavailable from Coleman et al. 1980).

These plots show that there is very good agreement between the predicted and observed counts. The plots also show that the brightest galaxies at any given color are indeed overwhelmingly dominated by early-type galaxies, so with a cut in apparent I magnitude indicated by the arrow, it should be possible to isolate a pure early-type subsample. The number of lens galaxies selected in each redshift interval (summed over all six pointings) using this magnitude cut may be found in Table 3. (In Fig. 1, the upper and right axes refer only to the early-type subsample. They show absolute B magnitude and luminosity function, i.e., number of galaxies $[h^{-1}\ \mathrm{Mpc}]^{-3}\,\mathrm{mag}^{-1}$.)

We can test the accuracy of these photometric redshifts using deep redshift surveys. Figure 2 shows the $V-I$ colors of Cowie's sample versus spectroscopic redshift. Superposed

TABLE 2

2dF Schechter Function Fits by Spectral Type

Type	M^B_*	α	$\phi_*[\times\ 10^{-3}(h^{-1}\ \mathrm{Mpc})^{-3}]$
E/S0.....	−19.61	−0.740	9.0
Sac	−19.53	−0.925	9.2
Scd	−19.00	−1.210	6.5

TABLE 3

Data

Lens Redshift	Number Lens	Number Pairs
0.1 ± 0.05.....	92	30896
0.2 ± 0.05.....	222	78928
0.3 ± 0.05.....	366	128533
0.4 ± 0.05.....	960	341541
0.5 ± 0.05.....	1611	580021
0.6 ± 0.05.....	663	237522
0.7 ± 0.05.....	699	255391
0.8 ± 0.05.....	594	216621
0.9 ± 0.05.....	233	84628
0.2 ± 0.15.....	680	238357
0.5 ± 0.15.....	3234	1159084
0.8 ± 0.15.....	1526	556640
0.5 ± 0.25.....	4299	1543008

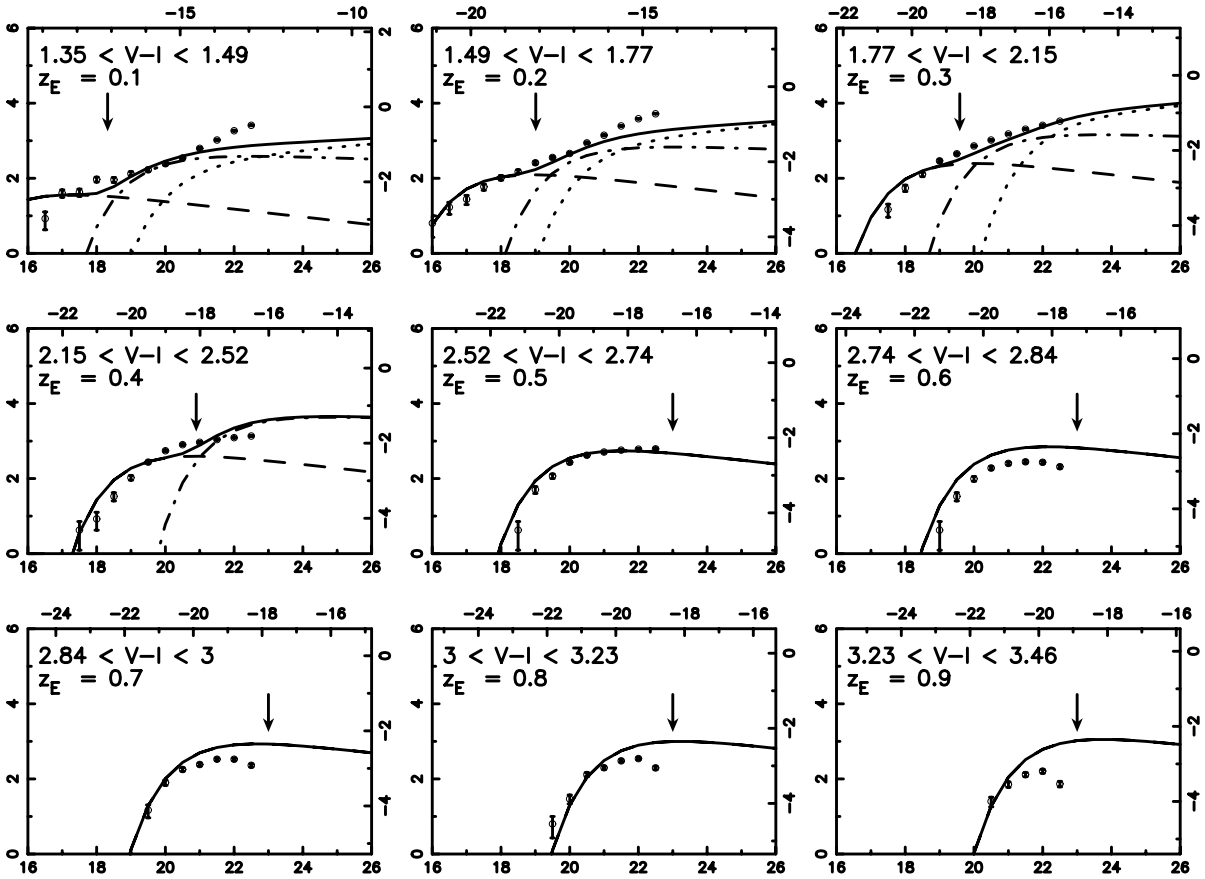

FIG. 1.—Symbols with error bars are the log counts (number of galaxies degree^{-2} mag^{-1}) vs. apparent I magnitude for galaxies in the color ranges indicated. Also shown are predictions for the contribution to the counts for E/SO (*dashed*), Sbc (*dot-dashed*), Scd (*dotted*), and cumulative (*solid*) galaxy types according to equation (15) and with Schechter function model parameters determined from the 2dF redshift survey (Folkes et al. 1999). The upper and right axes apply to early-type galaxies only and show absolute B magnitude and luminosity function (number of galaxies $[h^{-1}\ \mathrm{Mpc}]^{-3}$ mag^{-1}). The lines in these figures show that for colors corresponding to moderate redshift ellipticals ($0.1 \lesssim z \lesssim 0.4$ say), an L_* elliptical appears 2–3 mag brighter than an L_* spiral. Thus, by means of a suitable cut in magnitude—the value we have adopted is indicated by the arrow—one can isolate an essentially pure early-type sample. The $c(z)$ for spirals peaks at $z \simeq 1$ with $c \simeq 2.4$, and declines for higher z. This color corresponds to $z_E \simeq 0.4$, so for redder color there are no spirals. The good agreement between the predicted and observed counts in the elliptical dominated regime argues for little evolution of these galaxies. (There may be some disagreement with predictions at the highest redshifts because of slight evolution in L_* and/or some additional star formation blueing relative to nonevolving predictions).

are the color-redshift curves for the Coleman et al. (1980) SEDs. For red galaxies with $c > c_E(z = 0)$, the area of the symbol is proportional to the rest-frame B-band luminosity computed from the photometric redshift $z = z_E(c)$ and K correction $K = K_E[z_E(c)]$. This shows that the brightest galaxies at any given color do indeed lie along the upper envelope in color-redshift space delineated by the early-type locus.

Figure 3 shows the correspondence between spectroscopic and photometric redshift z_E for galaxies with $M_E < M_* + 1$. It shows very good agreement, with little scatter, though with a slight systematic offset at $z \sim 0.5$–1.0, which we interpret as an evolutionary effect.

2.3. *Background (Source) Galaxy Sample*

The background sample was selected to lie in a range of significance $4 < \nu < 150$ (equivalent to limiting magnitudes of $m_I \simeq 25$ and $m_I \simeq 21$ for a point source). The resulting number of source galaxies was 147,933. The number of lens-source pairs in each redshift interval (summed over all six pointings) is shown in Table 3. To make accurate predictions for the shear variance, it is necessary to have an accurate model for the redshift distribution for these faint galaxies or, more precisely, the distribution of weight over redshift. The measurements used here are not particularly deep, and there are nearly complete redshift samples that probe the required magnitude range. Here we shall use the SSA22 field sample of Cowie, which has the greatest depth and spectroscopic completeness.

In both I- and V-band samples, the weight is distributed over a range of several magnitudes, with half of the weight attributed to galaxies brighter/fainter than $m_I \simeq 23.0$ and $m_V \simeq 24.2$. The very faintest galaxies lie beyond the completion limit of Cowie's sample, but the redshift distribution in a band 1 mag wide about the median magnitude above is well determined. To a first approximation, the effect of variation of mean redshift with magnitude should cancel out, so we shall adopt the central-band redshift distribution as appropriate for the full sample. At this magnitude, the samples are approximately 80% complete, and it is thought that the galaxies for which a redshift cannot be obtained lie predominantly around $z = 1.5$–2.0.

We model the redshift distribution as

$$p(z) = 0.5z^2 \exp\,(-z/z_0)/z_0^3\,, \qquad (18)$$

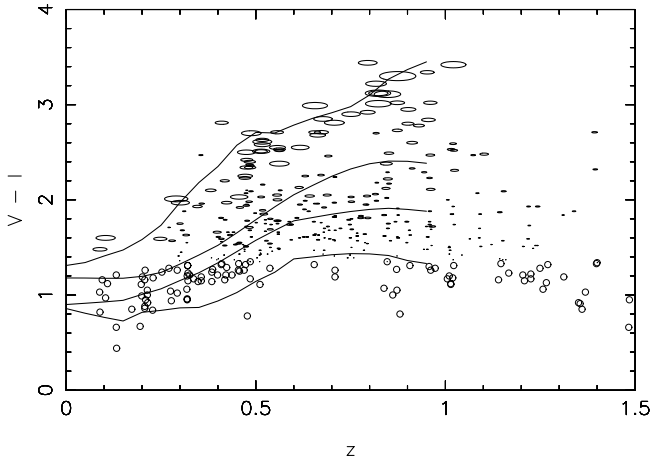

FIG. 2.—Lines show color vs. redshift computed from the Coleman et al. (1980) SEDs. From reddest (*top*) to bluest the lines represent E/SO, Sbc, Scd and Im galaxies. Symbols are measured colors and spectroscopic redshifts from Cowie. The sizes of the ellipses are proportional to the rest-frame absolute B luminosity of the galaxy computed using redshift $z_E(c)$ derived from the color assuming an early-type SED and with K correction $K_E[z_E(c)]$ for an early type at that color-redshift. Circles indicate galaxies that are bluer than a zero redshift elliptical. The key point here is that the symbol size is determined entirely from the broadband I, V colors, without any reference to the spectroscopic redshift. These show quite vividly that by selecting galaxies on this property, one obtains a sample of galaxies that are (1) with great probability early-type galaxies and (2) have a very tight color-redshift relation $c(z) \simeq c_E(z)$. The figure also reveals some minor, but interesting, discrepancies. There is a well-defined sequence of relatively blue galaxies at $z \sim 0.4$–0.7 that seem to track the spiral sequences, but lie $\simeq 0.2$ mag below the nonevolving spiral $c(z)$ prediction. This is probably caused by evolution but may also reflect in part some slight differences between the transmission functions for the standard system filters and those actually used at Keck and CFHT. Also, the redder galaxies at $z \sim 0.5$–1.0 again seem to be slightly bluer than the nonevolving predictions, and this results in a slight offset in the redshifts determined from the color.

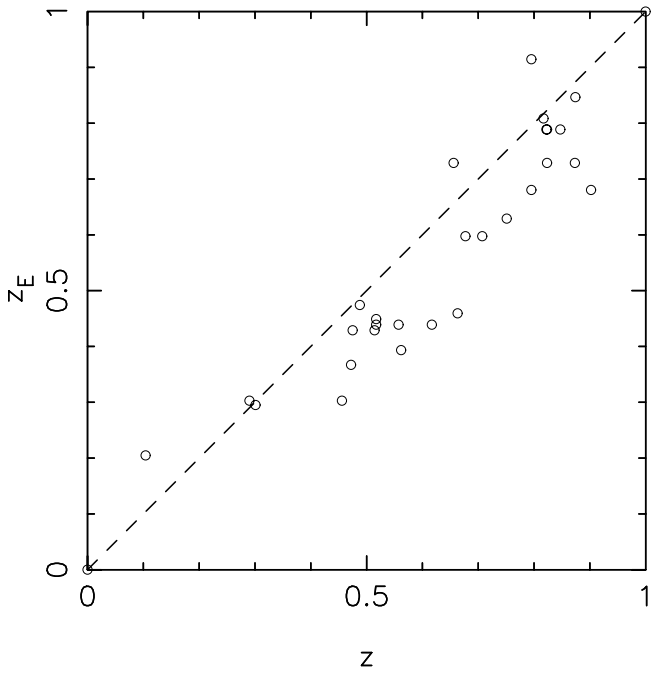

FIG. 3.—Photometric redshifts z_E for Cowie galaxies derived from $V-I$ color assuming nonevolving early-type SED. Only objects with $M_E < -18.6$ (1 mag fainter than M_*) are shown. There is very good agreement between these one-color photometric redshifts and the spectroscopic results. The color-derived redshifts—which assume there has been no evolution of the SED—appear to be systematically slightly low. This shift is in the sense expected if early-type galaxies at high redshift are slightly bluer than at the present epoch. See Fig. 2 for further discussion.

for which the mean redshift is $\bar{z} = 3z_0$ and the median redshift is $z_{\rm median} = 2.67z_0$. This is also the analytic form used by Wittman et al. (2000) and others, and it seems to adequately describe the data. To allow for incompleteness, we set the parameters n_0, z_0 of the model distribution to match the total number of galaxies in the Cowie sample (with and without secure redshifts) and to match the mean redshift with the unmeasurable objects assigned a redshift $z = 1.8$. Figure 4 shows the redshift distribution for galaxies around $m_I = 23.0$ along with the incompleteness corrected model, which has redshift scale parameter $z_0 = 0.39$. The same calculation for galaxies selected in a 1 mag wide band around $m_V = 24.2$ yields a slightly smaller, though very similar, redshift parameter $z_0 = 0.37$.

We now calculate $\langle\beta(z_l)\rangle$ as a function of lens redshift (see Tables 4 and 5 for the case of an Einstein–de Sitter universe). In Figure 5, we plot $\langle\beta\rangle$ as a function of lens redshift for three cosmologies. The dashed line is flat lambda ($\Omega_{m0} = 0.3$, $\Omega_{\lambda 0} = 0.7$), the solid line is Einstein–de Sitter ($\Omega_{m0} = 1.0$, $\Omega_{\lambda 0} = 0.0$), the dotted line is open baryon ($\Omega_{m0} = 0.05$, $\Omega_{\lambda 0} = 0.0$). Non-lambda cosmologies have very similar β values. Only the larger distances to source

TABLE 4

MODEL PARAMETERS FOR A FLAT LAMBDA ($\Omega_{m0} = 0.3$, $\Omega_{\lambda 0} = 0.7$) COSMOLOGY

Lens Redshift	$\langle\gamma_T\theta\rangle$ (20″–60″)	$\langle\beta(z_l)\rangle$	$(v/360\ {\rm km\ s^{-1}})^2$	$(L_{\rm eff}/L_*)^{1/2}_{\rm Direct}$	$(L_{\rm eff}/L_*)^{1/2}_{\rm Schechter}$	$(v_*/360\ {\rm km\ s^{-1}})^2$	v_*
0.1 ± 0.05.....	0.220 ± 0.222	0.849	0.278 ± 0.278	0.487	0.675	0.570 ± 0.570	272^{+113}_{-272}
0.2 ± 0.05.....	0.354 ± 0.146	0.711	0.533 ± 0.220	0.887	0.872	0.601 ± 0.248	279^{+53}_{-65}
0.3 ± 0.05.....	0.235 ± 0.111	0.589	0.427 ± 0.202	0.905	1.022	0.472 ± 0.223	247^{+53}_{-68}
0.4 ± 0.05.....	0.219 ± 0.068	0.484	0.485 ± 0.150	0.804	0.872	0.603 ± 0.187	279^{+40}_{-47}
0.5 ± 0.05.....	0.205 ± 0.055	0.395	0.556 ± 0.149	0.743	0.615	0.748 ± 0.201	311^{+39}_{-45}
0.6 ± 0.05.....	...	0.320	...	0.892	0.702	...	...
0.7 ± 0.05.....	0.050 ± 0.079	0.259	0.207 ± 0.327	1.065	0.808	0.194 ± 0.307	159^{+96}_{-159}
0.8 ± 0.05.....	0.210 ± 0.085	0.208	1.082 ± 0.438	1.244	0.946	0.870 ± 0.352	336^{+62}_{-77}
0.9 ± 0.05.....	...	0.167	...	1.419	1.127	...	...
0.2 ± 0.15.....	0.270 ± 0.082	0.664	0.435 ± 0.132	0.866	...	0.503 ± 0.153	255^{+36}_{-42}
0.5 ± 0.15.....	0.149 ± 0.038	0.406	0.393 ± 0.100	0.797	...	0.493 ± 0.126	253^{+30}_{-35}
0.8 ± 0.15.....	0.102 ± 0.053	0.225	0.485 ± 0.252	1.205	...	0.403 ± 0.209	228^{+53}_{-70}
0.5 ± 0.25.....	0.140 ± 0.033	0.398	0.377 ± 0.089	0.864	...	0.436 ± 0.103	238^{+27}_{-30}

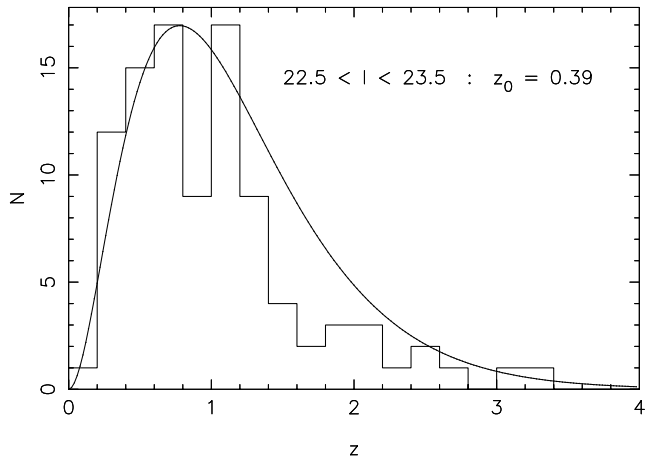

FIG. 4.—Histogram shows the observed distribution of redshifts from Cowie. The curve is a model that allows for incompleteness by assuming that $\simeq 20\%$ of unmeasurable galaxies lie at $z \simeq 1.8$.

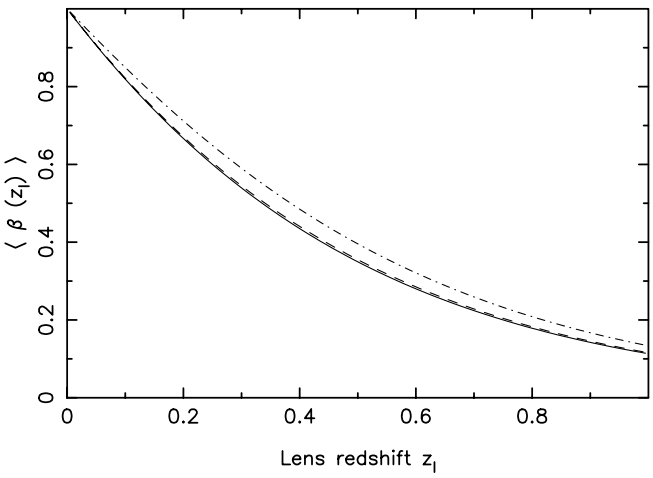

FIG. 5.—$\langle\beta(z_l)\rangle$ as a function of redshift and cosmology using the analytic approximation to an $m_I = 23$ source galaxy redshift distribution (Fig. 4). The solid line is Einstein–de Sitter ($\Omega_{m0} = 1.0, \Omega_{\lambda 0} = 0.0$), dotted is open baryon ($\Omega_{m0} = 0.05, \Omega_{\lambda 0} = 0.0$), dot-dashed is flat lambda ($\Omega_{m0} = 0.3, \Omega_{\lambda 0} = 0.7$). Non-lambda cosmologies have very similar $\langle\beta(z_l)\rangle$ values. Only the larger distances/volumes associated with lambda increase $\langle\beta(z_l)\rangle$ significantly for any given redshift.

galaxies associated with a cosmological constant increase β significantly at any lens redshift. We return to the dependence of halo mass on cosmology in § 4.

3. GALAXY DARK MATTER HALO MASSES

3.1. *Observed Tangential Shear Signal*

Having extracted a set of lens galaxies as described in § 2.2, we now compute the tangential shear averaged over lens-source pairs. However, not all lens galaxies will contribute equally to the shear signal. Insofar as galaxies have similar power-law mass density profiles, the massive lens galaxies cause more distortion of source galaxies in proportion to their mass. Therefore, to optimize the S/N, the shear contribution from each lens-source pair should be weighted by the mass of the lens. At small radii, the Faber-Jackson (Faber & Jackson 1976) relation tells us that the mass at a given radius scales as $\sqrt{L}$. Later work has shown that there is also an interdependence on a third parameter, the surface brightness of the galaxy, and that early types describe a "fundamental plane" (Djorgovski & Davis 1987; Dressler et al. 1987) or "fundamental band" (Guzman, Lucey, & Bower 1993). The Faber-Jackson correlation should be interpreted as a projection of this plane onto the mass-luminosity plane. However, the scatter introduced by neglecting surface brightness and by assuming that $M \propto \sqrt{L}$ is slight compared to other uncertainties in the analysis. Therefore, in the absence of information to the contrary, we shall assume that $M \propto \sqrt{L}$ (Guzman et al. conclude $M \propto L^{0.54}$), and we shall also assume that this dependence continues to larger radii. The weighted mean tangential shear is given by

$$\gamma_T(\theta) = \frac{\sum w\gamma_T}{\sum w} = \frac{\sum L^{1/2}\gamma_T}{\sum L^{1/2}}\,, \tag{19}$$

where the shear values have W_s (eq. [1]) incorporated.

This weighted tangential shear is plotted in Figure 6 for nine slices in lens redshift. The uncertainty (the variance in $\langle\gamma_T\rangle$) is calculated by rotating each source galaxy through 45°. The very highest and lowest redshift bins are rather noisy, but, in general, a positive signal is seen. As mentioned, for flat rotation curve halos the shear falls as $1/\theta$. Figure 7 shows the product $\theta\gamma_T$, which does indeed seem to be roughly independent of radius.

TABLE 5

MODEL PARAMETERS FOR AN EINSTEIN–DE SITTER ($\Omega_{m0} = 1.0, \Omega_{\lambda 0} = 0.0$) COSMOLOGY

Lens Redshift	$\langle\gamma_T\theta\rangle$ (20″–60″)	$\langle\beta(z_l)\rangle$	$(v/360\ \mathrm{km\ s^{-1}})^2$	$(L_{\rm eff}/L_*)^{1/2}_{\rm Direct}$	$(L_{\rm eff}/L_*)^{1/2}_{\rm Schechter}$	$(v_*/360\ \mathrm{km\ s^{-1}})^2$	v_*
0.1 ± 0.05.....	0.206 ± 0.233	0.819	0.269 ± 0.305	0.475	0.676	0.567 ± 0.641	271^{+125}_{-271}
0.2 ± 0.05.....	0.374 ± 0.158	0.667	0.601 ± 0.254	0.848	0.872	0.708 ± 0.299	303^{+58}_{-73}
0.3 ± 0.05.....	0.241 ± 0.133	0.540	0.478 ± 0.264	0.862	1.022	0.555 ± 0.306	268^{+66}_{-89}
0.4 ± 0.05.....	0.215 ± 0.080	0.435	0.529 ± 0.197	0.745	0.872	0.710 ± 0.264	303^{+52}_{-63}
0.5 ± 0.05.....	0.205 ± 0.055	0.350	0.628 ± 0.168	0.618	0.567	1.016 ± 0.273	363^{+46}_{-52}
0.6 ± 0.05.....	...	0.280	...	0.725	0.635	...	...
0.7 ± 0.05.....	0.050 ± 0.079	0.224	0.239 ± 0.378	0.849	0.712	0.282 ± 0.445	191^{+116}_{-191}
0.8 ± 0.05.....	0.210 ± 0.085	0.179	1.258 ± 0.509	0.973	0.808	1.293 ± 0.523	409^{+76}_{-94}
0.9 ± 0.05.....	...	0.142	...	1.092	0.929	...	...
0.2 ± 0.15.....	0.282 ± 0.093	0.630	0.479 ± 0.158	0.820	...	0.584 ± 0.193	275^{+42}_{-50}
0.5 ± 0.15.....	0.141 ± 0.040	0.354	0.426 ± 0.121	0.680	...	0.627 ± 0.178	285^{+38}_{-44}
0.8 ± 0.15.....	0.102 ± 0.053	0.194	0.563 ± 0.293	0.945	...	0.596 ± 0.310	278^{+65}_{-85}
0.5 ± 0.25.....	0.131 ± 0.035	0.343	0.409 ± 0.109	0.732	...	0.559 ± 0.149	269^{+34}_{-39}

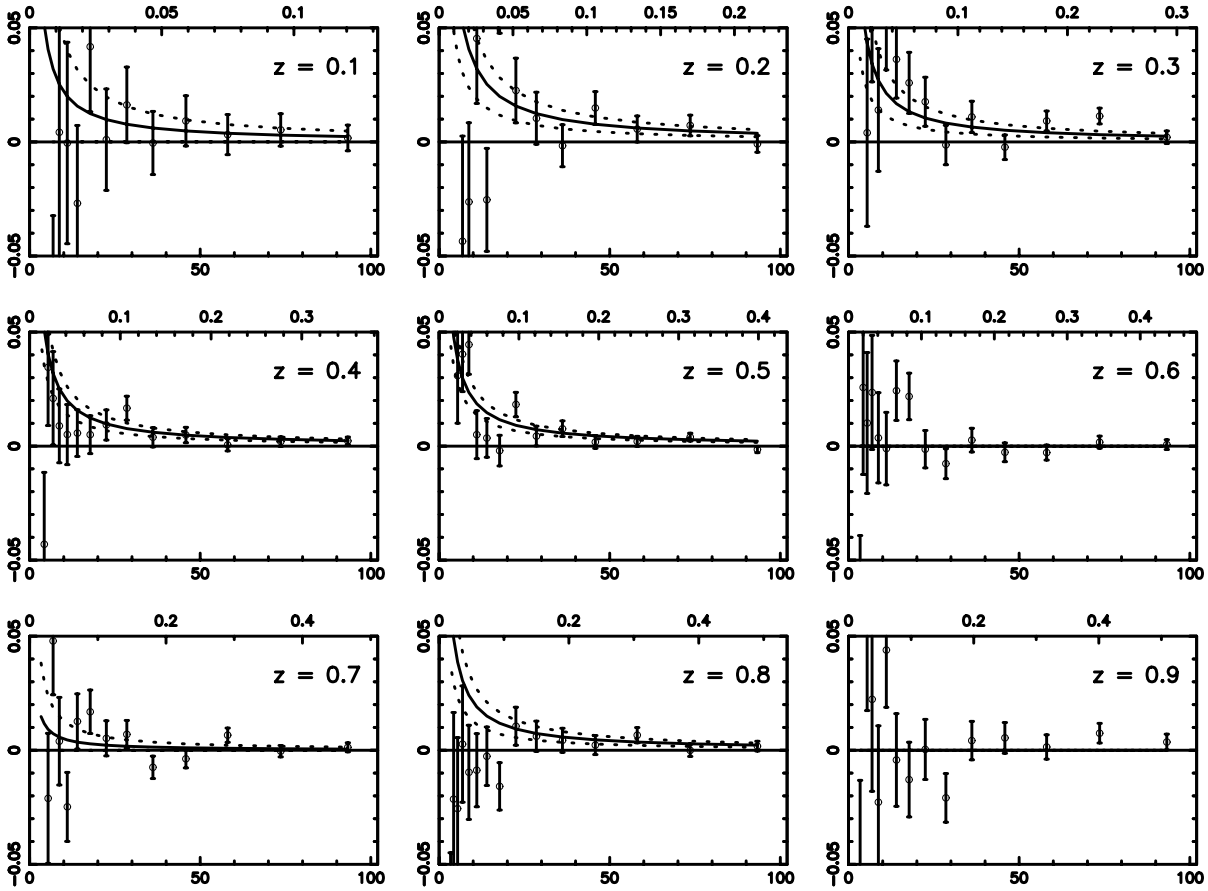

FIG. 6.—Mean tangential shear around early-type (lens) galaxies. The foreground galaxies have been color-selected and range in redshift from $z = 0.1$ to $z = 0.9$ in intervals of width $dz = 0.1$. The uncertainty has been calculated by rotating each source galaxy through 45°. Lower axis shows the lens-source galaxy projected radial separation in arcseconds. Upper axis shows the physical separation in h^{-1} Mpc at the lens redshift assuming a flat lambda universe. The solid (dotted) line is the best ($\pm 1\ \sigma$) fit to the data.

The solid (dotted) line(s) on Figures 6 and 7 shows the average $\theta\gamma_T$ ($\pm 1\ \sigma$). The signal appears to be noisy and unreliable at small angular separation, so we average points between 20″ and 60″. The best-fit $\theta\gamma_T$ value is quoted (where positive) for each redshift in Table 4. Also shown in the table are the equivalent mean rotation velocities obtained using the $\langle\beta(z_l)\rangle$ values computed above and in equation (8).

Since the $L_{\rm min}$ values vary with lens redshift because of the magnitude cut discussed in § 2.2, one cannot compare the different $\theta\gamma_T$ values directly (the lower redshift bins average over somewhat fainter galaxies). If, however, $M \propto L^{1/2}$, then the mean $\theta\gamma_T$, and the equivalent rotation velocity, are equal to that for some effective luminosity $L_{\rm eff}$. This effective luminosity can be computed in two ways: either as a direct sum over lens galaxies,

$$\left(\frac{L_{\rm eff}}{L_*}\right)^{1/2}_{\rm Direct} = \frac{\sum w(L/L_*)^{1/2}}{\sum w} = \frac{\sum L/L_*}{\sum (L/L_*)^{1/2}}\,, \qquad (20)$$

or by integrating over the luminosity function,

$$\left(\frac{L_{\rm eff}}{L_*}\right)^{1/2}_{\rm Schechter} = \frac{\int_{x_{\rm min}}^{\infty} x^{(1+\alpha)} \exp(-x)dx}{\int_{x_{\rm min}}^{\infty} x^{(0.5+\alpha)} \exp(-x)dx}\,, \qquad (21)$$

($x = L/L_*$), with parameters given by 2dF (Table 2). These give very similar results (Table 4), so we use the direct method henceforth.

Finally, given v and $(L_{\rm eff}/L_*)^{1/2}$ one can compute the equivalent mean rotation velocity for an L_* lens galaxy:

$$v_*^2 = v^2/(L_{\rm eff}/L_*)^{1/2}\,. \qquad (22)$$

This result is again strictly dependent on the assumption that masses scale as $\sqrt{L}$, but given the limited range of absolute magnitudes used here the result is only weakly dependent on this assumption. The last two columns of Table 4 show $(v_*/360\ {\rm km\ s^{-1}})^2 = (v/360\ {\rm km\ s^{-1}})^2/(L_{\rm eff}/L_*)^{1/2}$ and, hence, v_* at each redshift.

While the narrow ($\Delta z = 0.1$) bins here give very good resolution in redshift, the limited number of lens galaxies in each bin results in quite noisy results. To enhance the S/N, at the expense of a slight loss in redshift resolution, we now rebin the signal using coarser redshift bins. Figures 8 and 9 show the mean tangential shear signal, γ_T and $\theta\gamma_T$, using redshift bins of $dz = 0.3$ in first three panels. Note that by combining our data in this way we are summing over slightly different physical scales. In Table 4 we again calculate $(v_*/360\ {\rm km\ s^{-1}})^2 = (v/360\ {\rm km\ s^{-1}})^2/(L_{\rm eff}/L_*)^{1/2}$ and also v_*. We obtain values of $v_* = 255^{+36}_{-42}$ for $z = 0.2 \pm 0.15$, $v_* = 253^{+30}_{-35}$ for $z = 0.5 \pm 0.15$, and $v_* = 228^{+53}_{-70}$ for $z = 0.8 \pm 0.15$. Thus, it appears that there is little evolution in the mass of dark matter halos with redshift. In the final panel of Figures 8 and 9, we bin the signal for lens galaxies between $z = 0.25$ and $z = 0.75$. We conclude that $v_* = 238^{+27}_{-30}$ for $z = 0.5 \pm 0.25$.

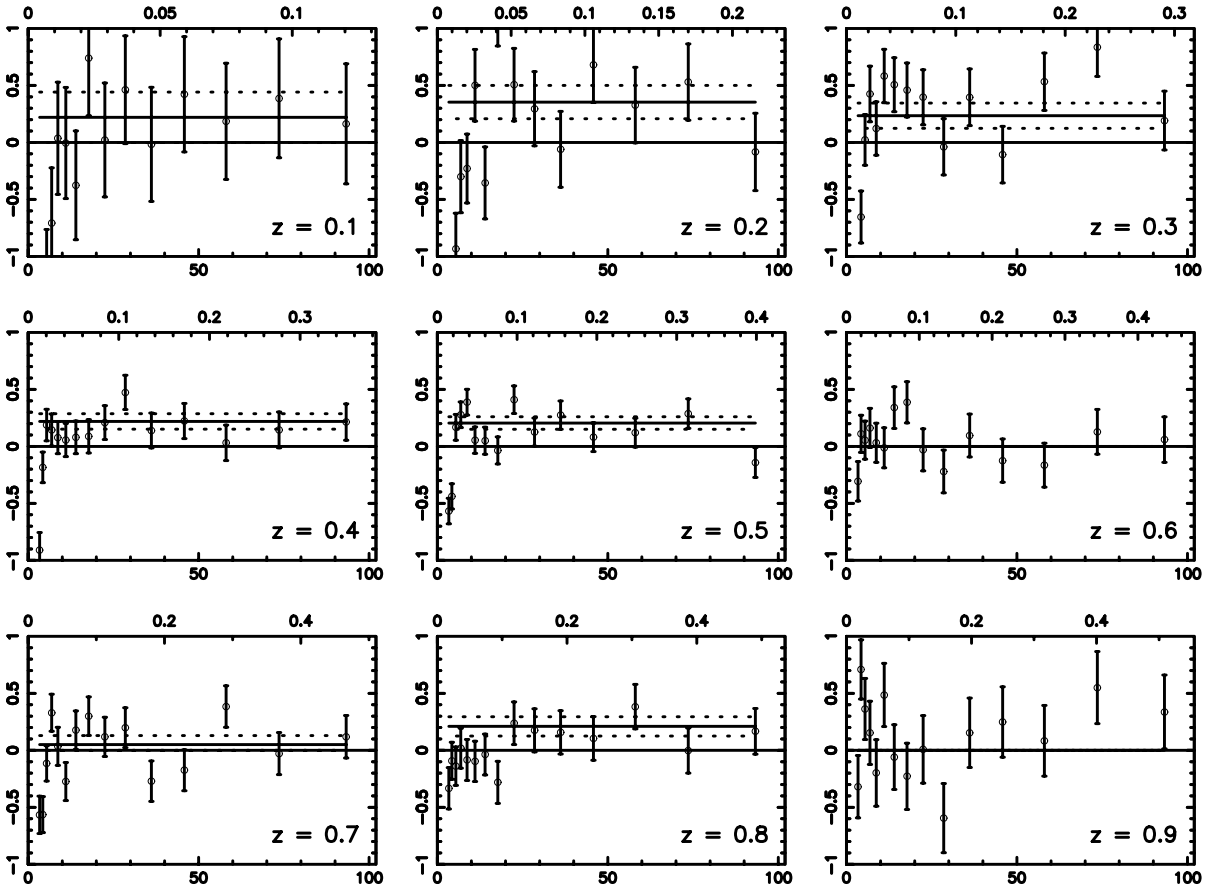

FIG. 7.—Product of mean tangential shear around early-type (lens) galaxies and lens-source galaxy projected radial separation in arcseconds. The foreground galaxies have been color-selected and range in redshift from $z = 0.1$ to $z = 0.9$ in intervals of width $dz = 0.1$. The uncertainty has been calculated by rotating each source galaxy through 45°. Lower axis shows the lens-source galaxy projected radial separation in arcseconds. Upper axis shows the physical separation in h^{-1} Mpc at the lens redshift assuming a flat lambda universe. The solid (dotted) line is the best ($\pm 1\ \sigma$) fit to the data.

The signal strength that is being measured is small. As a check for systematic errors, in Figure 10 we use the same data as in Figure 9 but rotate the galaxies through 45°. As expected, there is no resultant signal causing us to conclude that systematic errors are negligible. (The interested reader is referred to Paper I for a description of our careful corrections for systematics.)

4. DISCUSSION

In the previous sections we have shown that with our *I*- and *V*-band CFHT data we can select a sample of bright early-type galaxies, determine their redshifts to a reasonable degree of precision, and measure the shear that they produce in faint background galaxies over quite a range of angular scales and lens redshifts. We find little evolution of the halos with redshift. We also find that the radial dependence of the shear is consistent with roughly flat rotation curve halos. Our results imply mean rotation velocities for L_* galaxy halos at $r \sim 50$–$200\ h^{-1}$ kpc of $v_* = 238^{+27}_{-30}$ km s^{-1}. This number is dependent on the assumption that the mass at a given radius scales as the square root of the luminosity, as is known to be the case at much smaller scales from the Faber-Jackson relation. However, since our lens galaxy sample is restricted to relatively bright galaxies—within a magnitude or so of L_*—we expect this dependence to be rather weak. We now discuss some of the implications of this result. We compute the mass-to-light ratio and the contribution to the total density from these halos. We compare our results with dynamical measurements at smaller scales, with X-ray and other lensing measurements at similar scales to these we can reliably measure. We also compare the properties of these halos to those found in numerical cosmological simulations. Finally, we discuss uncertainties caused by evolution and cosmology.

4.1. *M/L and Contribution to* Ω_0

An L_* galaxy halo with $v_* = 238$ contains $1.31 \times 10^{12}(r/100\ h^{-1}\ \mathrm{kpc})h^{-1}\ M_\odot$ within a radius of r since $M(r) = v_*^2 r/G$. An L_* galaxy has a luminosity of $1.09 \times 10^{10}\ h^{-2}\ L_\odot^B$, so the mass-to-light ratio is $M/L_B = 121 \pm 28\ h(r/100\ h^{-1}\ \mathrm{kpc})$, or about $M/L_B \sim 250\ h$ at the outermost points we can reliably measure.

We can compute the contribution of these halos to the total density of the universe. This is, of course, only a partial contribution since only early-type galaxies are counted—though they may well in fact account for the majority of the mass—and because here we have deliberately restricted attention to relatively small scales $\lesssim 200\ h^{-1}$ kpc. We shall assume, as above, that $M \propto \sqrt{L}$, so

$$M(r) = M_*(r)\sqrt{L/L_*}\ , \tag{23}$$

where $M_*(r)$ is the mass profile for an L_* galaxy, and the

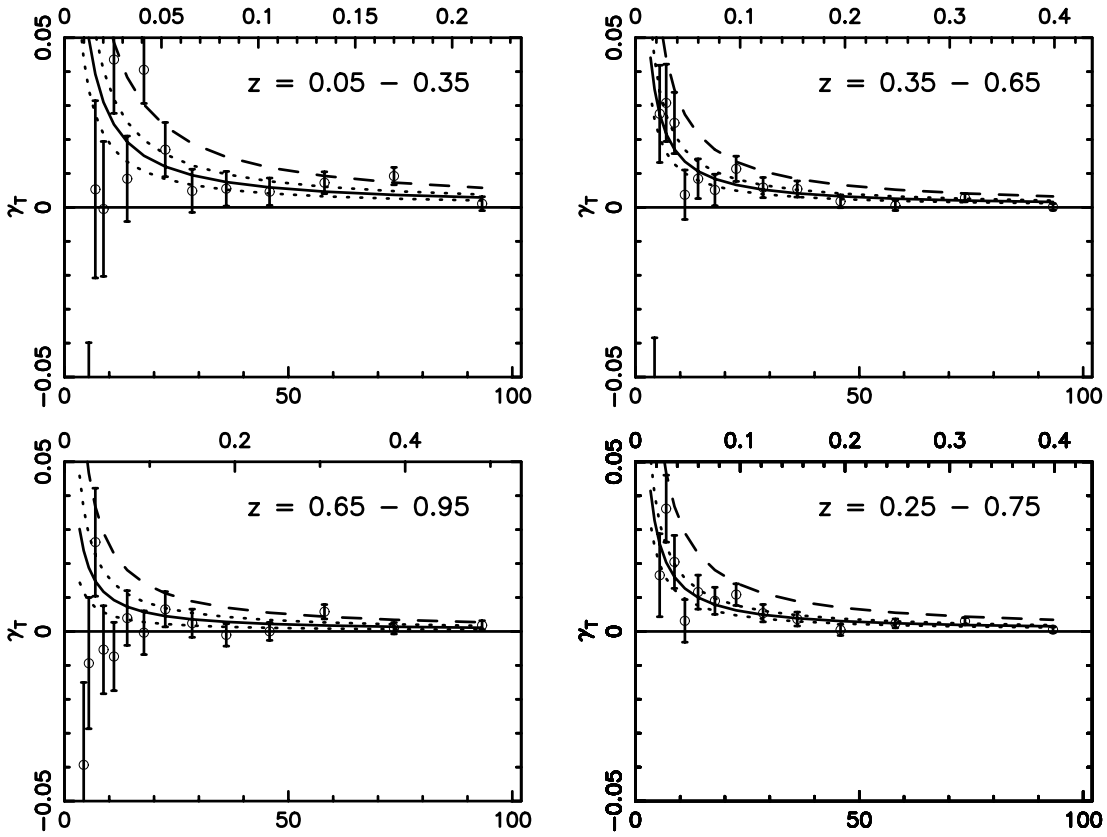

FIG. 8.—Same as Fig. 6 but for a broader redshift range as indicated on each panel. The solid (dotted) line is the best ($\pm 1\,\sigma$) fit to the data. The dashed line is the predicted shear if small-scale values of rotation velocity from dynamical measurements are extrapolated to larger scales as discussed in § 4.2.

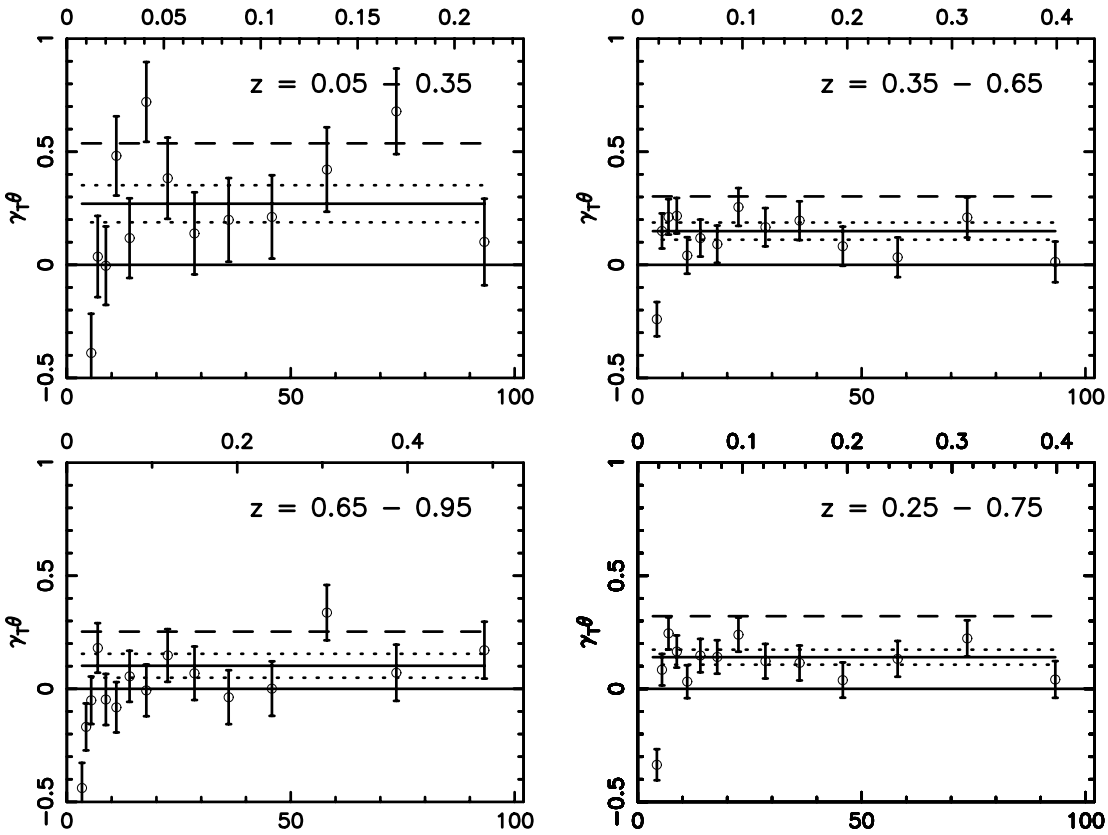

FIG. 9.—Same as Fig. 7 but for a broader redshift range as indicated on each panel. The solid (dotted) line is the best ($\pm 1\,\sigma$) fit to the data. The dashed line is the predicted shear if small-scale values of rotation velocity from dynamical measurements are extrapolated to larger scales as discussed in § 4.2.

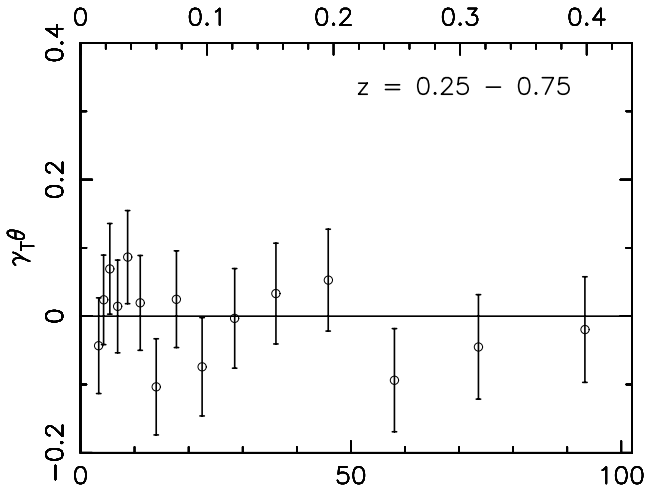

FIG. 10.—Same as Fig. 9 but with galaxies rotated through 45°. The signal has disappeared as expected.

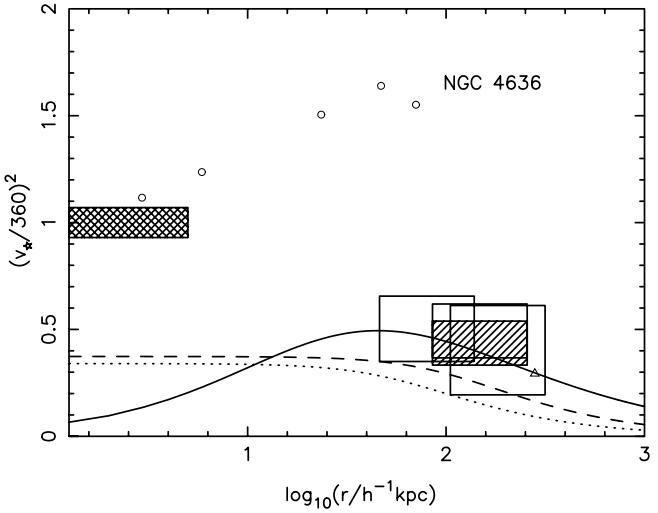

FIG. 11.—Square of rotation velocity as a function of radius. The hashed rectangle is the value determined for the central region of an L_* galaxy (Fukugita & Turner 1991). The three outlined rectangles are the values obtained from this work (Table 4) for an L_* galaxy at redshifts 0.2, 0.5, 0.8 ± 0.15. The striped rectangle is the value from this work (Table 4) for an L_* galaxy at redshift 0.5 ± 0.25. The circles are the values determined by Mushotzky et al. (1994) from X-ray measurements of NGC 4636 (assuming $H_0 = 70$ km s^{-1} Mpc^{-1}). The triangle is the value of halo mass from Jenkins et al. (2001) with the same abundance as an L_* galaxy. The solid line is the rotation curve for an NFW profile (Navarro et al. 1997) with normalization parameter chosen to intercept the triangle. The dashed and dotted lines are the best fits from Brainerd et al. (1996) and Hudson et al. (1998) to a parametric model for *late* types.

density is then

$$\rho = M_*(r)\int dL\ \phi_E(L)\sqrt{L/L_*} = M_*(r)\phi_{E*}\,\Gamma(\alpha + 3/2)\ . \quad (24)$$

With the numbers from Table 2, we find this constitutes $\Omega = 0.04 \pm 0.01(r/100\ h^{-1}\ \mathrm{kpc})$ of closure density.

4.2. *Comparison with Small-Scale Dynamics*

Stellar velocity dispersions in ellipticals probe the mass on scales of a few kpc—much smaller than the scales we are measuring—and yield the Faber-Jackson relationship (that $L \propto \sigma_v^4$; Faber & Jackson 1976). A distillation of these and later studies by Fukugita & Turner (1991) gives $\sigma_{v*} = 210$ km s^{-1} (the mean of their E/S0 line-of-sight stellar velocity dispersions). If we assume that the stars are test particles on finite orbits in a roughly flat rotation curve halo, the L_* rotation velocity at a scale of a few kpc is then $\sqrt{3} \times 210 \simeq 360$ km s^{-1}. The corresponding mass is larger by a factor of 2–3 than the value we measure on scales of 50–200 h^{-1} kpc. For interest, in Figures 8 and 9 we plot (*dashed line*) the signal that would be obtained from a galaxy with the same effective luminosity $(L_{\mathrm{eff}}/L_*)^{1/2}$ (Table 4) as our galaxies but with the rotation velocity of 360 km s^{-1} (the value determined on small scales from Faber-Jackson measurements). Clearly, in all cases, the predicted signal is larger than the measured signal. Thus, while both small- and large-scale measurements are individually consistent with flat rotation curves, if we combine them they suggest that the mean density profiles are actually falling off slightly faster than $\rho \propto r^{-2}$. If we say that our measurements are probing radii a factor ~ 30 larger than the stellar dynamical measurements, and that our v^2 is about 2.3 times smaller, then the mean profile over this range is $\rho \propto r^{-(2+\epsilon)}$ with $\epsilon = \ln(2.3)/\ln(30) \simeq 0.24$, so $\rho \propto r^{-2.2}$. Note that such a small departure from a pure flat rotation curve would be impossible to detect from either set of measurements alone. Neither does the small departure from $\rho \propto r^{-2}$ seriously invalidate, e.g., equation (8).

In Figure 11 we plot various rotation velocity estimates as a function of radius. The hashed rectangle at the smallest scale on Figure 11 is from Fukugita & Turner. The three outlined rectangles are the values from this work (Table 4) for an L_* galaxy at redshifts 0.2, 0.5, 0.8 ± 0.15. The striped rectangle is the values from this work (Table 4) for an L_* galaxy at redshift 0.5 ± 0.25.

4.3. *Comparison with X-Ray Halos*

As discussed in § 1, elliptical galaxy halo masses have been determined in a small number of cases from X-ray observations. In the best-studied case of NGC 4636 (Mushotzky et al. 1994), the mass is very large and grows with radius faster than $M \propto r$ out to $r \sim 100$ kpc. These results are shown as circles in Figure 11 (assuming $H_0 = 70$ km s^{-1} Mpc^{-1}). If representative of elliptical galaxies in general, this would have weighty implications (Bahcall, Lubin, & Dorman 1995). However, there is clearly some question as to whether these galaxies, which have abnormally bright and extended X-ray emission are typical. Our results strongly suggest that NGC 4636 is indeed an atypical object, being far more massive than typical elliptical galaxies, and consequently that the contribution of these galaxies to the Bahcall et al. accounting needs to be revised substantially downward by a factor or 2–3.

4.4. *Comparison with Cosmological Simulations*

We now compare the properties of elliptical galaxy halos with halos of the same abundance in numerical cosmological simulations. This should be a valid test of theoretical models since we have measured the mass on scales that should be accurately modeled on the computer and should be little affected by gas dynamics and star formation.

With the 2dF luminosity function parameters, the number density of ellipticals brighter than L_* is

$$N(>L_*) = \phi_*\int_1^\infty dy\ y^\alpha e^{-y} \simeq 0.25\ \phi_* \simeq 2.2 \times 10^{-3}\ h^3\ \mathrm{Mpc}^{-3}\ . \quad (25)$$

The differential mass function from the high resolution ΛCDM simulations of Jenkins et al. (2001, their Fig. 2) probe the relevant mass scales. Integrating these to obtain the cumulative mass function, we find that $N(>M) = N(>L_*)$ for $M \simeq 2.44 \times 10^{12}\, h^{-1}\, M_\odot$. The mass here is the mass for an overdensity of 324, which, with $\Omega_{m0} = 0.3$, corresponds to radius of $r \simeq 279\ h^{-1}$kpc and to a rotation velocity at that radius of $v \simeq 194$ km s^{-1} (shown by the triangle in Fig. 11). Navarro, Frenk, & White (1997) find that halos in this mass range in their ΛCDM simulations are well described by their universal model with concentration parameter $c \simeq 10$ (their Fig. 6), and to match Jenkins et al. rotation velocity requires $v_{200} \simeq 210$ km s^{-1}. The rotation curve profile for such a model is shown as the solid line in Figure 11 and matches our measured values extremely well.

This comparison—simply matching the cumulative number density of halos to that of an $L > L_*$ elliptical—should not be considered definitive, but it is the best one can do with the published numerical results. This comparison could be improved by using semianalytic galaxy formation to identify plausible candidates for elliptical galaxies and then computing the average mass profile around these.

4.5. *Comparison with other Galaxy-Galaxy Lensing Studies*

A number of other groups have measured v_* from galaxy-galaxy lensing. Early studies had low S/N and results were typically presented as constraints on parameterized models. Values of $v_* = 220 \pm 80$ km s^{-1} (Brainerd et al. 1996), $v_* = 262^{+42}_{-49}$ km s^{-1} (Dell'Antonio & Tyson 1996), and $v_* = 210 \pm 40$ km s^{-1} (Hudson et al. 1998) were obtained. Dell'Antonio & Tyson measured a signal on very small scales (within a projected radius of 5″) so their value is not directly comparable to that obtained here. Brainerd et al. and Hudson et al. both used the same parametric model for halo mass (eq. [3.4] of Brainerd et al.). In Figure 11, we plot rotation velocity with radius using the best-fit solution from Brainerd et al. (*dashed line*) and of Hudson et al. (*dotted line*). It should be noted that Brainerd et al. (1996), Dell'Antonio & Tyson (1996), and Hudson et al. (1998) were all measuring halo rotation velocities for primarily late-type galaxies and one would expect lower values for their halo masses than those obtained from our measurements for early-type galaxies. (Fukugita & Turner [1991] find $v_* = 204$ km s^{-1} for late-type galaxies from the Tully-Fisher [Tully & Fisher 1977] relationship.)

Fischer et al. (2000) were the first group to obtain sufficiently high S/N to fit a power law directly to their data. Using preliminary data from the Sloan Digital Sky Survey, they obtained a signal out to several hundred arcseconds and measured a rotation velocity of $v_* = 240 \pm 28$ km s^{-1}. (Note that the uncertainty here is a 95% confidence limit not a 1 σ uncertainty as for the other groups.) The interpretation of their results is somewhat complex because their lens sample is a mixture of early and late types, but the power and potential of galaxy-galaxy lensing was convincingly demonstrated.

4.6. *Uncertainties caused by Evolution and Cosmology*

The analysis in this paper assumed that L_* does not evolve with redshift. Based on our knowledge of early-type galaxy evolution with redshift, this does not seem a grossly inaccurate assumption. From the Canada-France redshift survey, Lilly et al. (1995) found that their red (redder than present-day Sbc and, hence, early-type galaxies) sample was consistent with no change in L_* between $z \sim 0.8$ and $z \sim 0.3$ (their red sample was also consistent with a change of *at most* a few tenths of a magnitude).

We note that a brightening of 0.5 mag in L_* for the highest redshift sample ($z = 0.8 \pm 0.15$) (which might be feasible because of passive evolution) would induce a small ($\sim$25%) increase in v_*^2.

We assumed a flat lambda cosmology. If, for example, we had assumed an Einstein–de Sitter cosmology (Table 5) in preference to flat lambda, the inferred values of v_* would still be approximately constant with redshift but would increase to $v_* = 275^{+42}_{-50}$ km s^{-1} for $z = 0.2 \pm 0.15$, $v_* = 285^{+38}_{-44}$ km s^{-1} for $z = 0.5 \pm 0.15$, and $v_* = 278^{+65}_{-85}$ km s^{-1} for $z = 0.8 \pm 0.15$. The increase in v_* in such a universe is caused primarily by smaller $\langle\beta\rangle$ values in this cosmology (Table 5 and Fig. 5). We would conclude a rotation velocity of $v_* = 269^{+34}_{-39}$ km s^{-1} for $z = 0.5 \pm 0.25$ for this cosmology.

5. CONCLUSIONS

Unlike previous galaxy-galaxy lensing analyses, we showed that it was possible to use colors and magnitudes to cleanly select one type of lens galaxy (in this case, bright early-type galaxies). By measuring a weighted mean tangential shear, which decreased roughly as $1/\theta$, we concluded that early-type galaxies have approximately flat rotation curve halos extending out to several hundred h^{-1} kpc. By assuming an $M \propto L^{1/2}$ relationship, we inferred a rotation velocity for an L_* galaxy of $v_* = 238^{+27}_{-30}$ km s^{-1} for a flat lambda ($\Omega_0 = 0.3$, $\lambda_0 = 0.7$) cosmology ($v_* = 269^{+34}_{-39}$ km s^{-1} for Einstein–de Sitter) with little evidence for evolution with redshift. These halo masses are somewhat (2–3 times) lower than a simple perfectly flat rotation curve extrapolation from small-scale dynamical measurements. They are also considerably lower than the masses of halos found from the best studied X-ray halos, although we note that the best X-ray example is likely an atypical object. Interestingly, the values of halo mass determined from galaxy-galaxy lensing and the masses of halos of the same abundance in lambda-CDM simulations agree remarkably well. We note, however, that for an optimum comparison, halo masses should be determined as a function of redshift directly from the simulations.

Finally, we determined a mass-to-light ratio for galaxy halos of $M/L_B = 121 \pm 28\ h(r/100\ h^{-1}$ kpc) (for L_* galaxies) and found that these halos constitute $\Omega \simeq 0.04 \pm 0.01(r/100\, h^{-1}$ kpc) of closure density.

In the foreseeable future, it will be possible to measure early-type galaxy halo masses rather more precisely. The color-redshift degeneracy (illustrated by Fig. 1) could be broken by the availability of a larger number of passbands to provide photometric redshifts such as will be provided by the Hawaii Lensing Survey, the Deep Lens Survey, or the Megacam/Terapix consortium. More preferable would be spectroscopic redshift determinations such as will be provided by the Sloan Digital Sky Survey. The greater range of absolute luminosity then available (limited here to $M \sim M_* \pm 1$) will allow mass-to-luminosity dependence (assumed in this work to be $M \propto \sqrt{L}$) to be determined more precisely. Moreover, increased numbers of early-type lens galaxies will reduce uncertainties in the measurement of tangential shear and allow any variation in a $1/\theta$ (i.e., flat) rotation

curve galaxy halo profile to be determined. Finally, the availability of greater than two-passband data will also allow photometric redshifts for late-type galaxies and a similar investigation to be undertaken into the properties of their halos.

G. W. gratefully acknowledges financial support from the estate of Beatrice Watson Parrent and from Mr. & Mrs. Frank W. Hustace, Jr., while Parrent Fellow at the University of Hawaii. This work was supported by NSF grant AST 99-70805.

REFERENCES

Bahcall, N. A., Lubin, L. M., & Dorman, V. 1995, ApJ, 447, L81
Bahcall, J. N., & Tremaine, S. 1981, ApJ, 244, 805
Bosma, A. 1981, AJ, 86, 1825
Brainerd, T. G., Blandford, R. D., & Smail, I. 1996, ApJ, 466, 623
Coleman, G. D., Wu, C., & Weedman, D. W. 1980, ApJS, 43, 393
Cowie, L. L., Gardner, J. P., Hu, E. M., Songaila, A., Hodapp, K. W., & Wainscoat, R. J. 1994, ApJ, 434, 114
Cowie, L. L., Songaila, A., & Barger, A. J. 1999, AJ, 118, 603
Cowie, L. L., Songaila, A., Hu, E. M., & Cohen, J. G. 1996, AJ, 112, 839
Davis, M., & Peebles, P. J. E. 1983, ApJ, 267, 465
Dell'Antonio, I. P., & Tyson, J. A. 1996, ApJ, 473, L17
Djorgovski, S., & Davis, M. 1987, ApJ, 313, 59
Dressler, A., Lynden-Bell, D., Burstein, D., Davies, R. L., Faber, S. M., Terlevich, R., & Wegner, G. 1987, ApJ, 313, 42
Faber, S. M., & Gallagher, J. S. 1979, ARA&A, 17, 135
Faber, S. M., & Jackson, R. E. 1976, ApJ, 204, 668
Fischer, P., et al. 2000, AJ, 120, 1198
Folkes, S., et al. 1999, MNRAS, 308, 459
Fukugita, M., & Turner, E. L. 1991, MNRAS, 253, 99
Griffiths, R. E., Casertano, S., Im, M., & Ratnatunga, K. U. 1996, MNRAS, 282, 1159
Guzman, R., Lucey, J. R., & Bower, R. G. 1993, MNRAS, 265, 731
Hudson, M. J., Gwyn, S. D. J., Dahle, H., & Kaiser, N. 1998, ApJ, 503, 531
Jenkins, A., Frenk, C. S., White, S. D. M., Colberg, J. M., Cole, S., Evrard, A. E., Couchman, H. M. P., & Yoshida, N. 2001, MNRAS, 321, 372
Jing, Y. P., Mo, H. J., & Boerner, G. 1998, ApJ, 494, 1
Kaiser, N. 1991, in New Insights into the Universe, ed. V. J. Martinez, M. Portilla, & D. Saez (New York: Springer), 279
———. 2000, ApJ, 537, 555
Kaiser, N., Squires, G., Fahlman, G., & Woods, D. 1994, in Clusters of Galaxies, ed. F. Durret, A. Mazure, & J. T. T. Van (Gif-sur-Yvette: Editions Frontières), 269
Kaiser, N., Wilson, G., & Luppino, G. 2001a, preprint (astro-ph/0003338) (Paper I)
Kaiser, N., Wilson, G., Luppino, G., & Dahle, H. 2001b, preprint (astro-ph/9907229)
Kaiser, N., Wilson, G., Luppino, G., Kofman, L., Gioia, I., Metzger, M., & Dahle, H. 2001c, preprint (astro-ph/9809268)
Kim, D., & Fabbiano, G. 1995, ApJ, 441, 182
Kovner, I., & Milgrom, M. 1987, ApJ, 321, L113
Lilly, S. J., Tresse, L., Hammer, F., Crampton, D., & Le Fevre, O. 1995, ApJ, 455, 108
Mellier, Y. 1999, ARA&A, 37, 127
Mushotzky, R. F., Loewenstein, M., Awaki, H., Makishima, K., Matsushita, K., & Matsumoto, H. 1994, ApJ, 436, L79
Natarajan, P., Kneib, J., Smail, I., & Ellis, R. S. 1998, ApJ, 499, 600
Navarro, J. F., Frenk, C. S., & White, S. D. M. 1997, ApJ, 490, 493
Trimble, V. 1987, ARA&A, 25, 425
Trinchieri, G., Fabbiano, G., & Kim, D. 1997, A&A, 318, 361
Trinchieri, G., Kim, D., Fabbiano, G., & Canizares, C. R. C. 1994, ApJ, 428, 555
Tully, R. B., & Fisher, J. R. 1977, A&A, 54, 661
Turner, E. L. 1976, ApJ, 208, 304
Tyson, J. A., Valdes, F., Jarvis, J. F., & Mills, A. P. 1984, ApJ, 281, L59
Wilson, G., Kaiser, N., & Luppino, G. 2001, ApJ, in press (Paper III)
Wittman, D. M., Tyson, J. A., Kirkman, D., Dell'Antonio, I., & Bernstein, G. 2000, Nature, 405, 143
Zaritsky, D., Smith, R., Frenk, C., & White, S. D. M. 1997, ApJ, 478, 39